Slowed Singlet Exciton Fission Enhances Triplet Exciton Transport in Select Perylenediimide Crystals

Tanner S. Volek,[1] Max A. Verkamp,[1,3] Gabriella N. Ruiz,[1] Alexander J. Staat,[2] Boxi Cam Li,[1] Michael J. Rose,[1] Joel D. Eaves,[2] & Sean T. Roberts[1,*]

[1]*Department of Chemistry, The University of Texas at Austin, Austin, TX 78712, USA*
[2]*Department of Chemistry, University of Colorado Boulder, Boulder, CO 80309, USA*
[3]*Department of Chemistry, Hanover College, Hanover, IN, 47243, USA*

Abstract

Singlet fission (SF) materials used in light-harvesting devices must not only efficiently produce spin-triplet excitons but also transport them over hundreds of nanometers. N,N'-bis(2-phenylethyl)-3,4,9,10-perylenedicarboximide (EP-PDI) is a promising SF chromophore due to its photostability, large extinction coefficient, and high triplet yield, but the energy transport mechanisms in EP-PDI solids are minimally understood. Herein, we use transient absorption microscopy to directly characterize exciton transport in EP-PDI crystals. We find evidence for singlet-mediated transport in which pairs of triplet excitons undergo triplet fusion (TF), producing spin-singlet excitons that rapidly diffuse. This interchange of singlet and triplet excitons shuttles triplets as far as 205 nm within the first 500 ps after photoexcitation. This enhanced transport comes at a cost, however, as it necessitates favoring triplet recombination and thus requires a fine-tuning of SF dynamics to balance triplet yields with triplet transport lengths. Through numerical modeling, we predict that tuning the ratio of SF and TF rate constants, k_{SF}/k_{TF}, to between 1.9 and 3.8 allows for an optimized triplet transport length (425 – 563 nm) with minimal loss (7 – 10%) in triplet yield. Interestingly, by adjusting the size of EP-PDI crystals we find we can subtly tune their crystal structure and thereby alter their SF and TF rates. By slowing SF within small EP-PDI crystals, we are able to boost their triplet transport length by ~20%. Although counter-intuitive, our work suggests that slowing SF by introducing moderate structural distortions can be preferential when optimizing triplet exciton transport, provided singlet exciton transport is not significantly hindered.

TOC Graphic

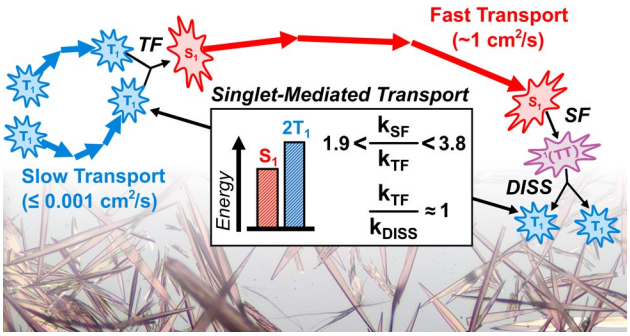

Introduction

Singlet fission (SF) is a multiple exciton generation process in which two spin-triplet excitons are produced when a lone spin-singlet exciton divides its energy between neighboring molecules.[1,2] This phenomenon occurs in a wide range of organic materials[3–9] wherein triplet yields near the theoretical maximum of 200% have been reported.[6,10–13] Because of this, SF has garnered great interest in light-harvesting applications as a route for overcoming the Shockley-Queisser limit.[14–16] A light absorbing layer made of a SF-material, connected optically in series with a single-junction solar cell, would serve to increase the power conversion efficiency of the device by doubling the excitons generated per photon absorbed and minimizing losses from hot carrier relaxation.[15,17–20] For such a device to work however, triplet excitons generated by SF must migrate through the SF absorber to reach a semiconductor junction where they can dissociate into charge carriers and contribute to the quantum efficiency of the device.[20–22] In recent SF-solar cell devices though, slow triplet exciton transport has restricted device thicknesses to be within the triplet diffusion length of the SF-material.[23–27] Since triplet diffusion lengths in thin films (L_D ~ 0.01 – 0.1 μm)[26,28] are often significantly shorter than the film's optical absorption depth (L_A ~ 0.2 – 1.2 μm)[29–32] device performances suffer from inadequate light absorption[32,33] and singlet exciton dissociation,[34,35] preventing them from reaching expected external quantum efficiencies. It is therefore of great importance to study both the efficient production of triplet excitons by SF and their subsequent transport, developing design principles that optimize both processes concertedly.

In a simple three state kinetic model of SF, a spin-correlated triplet-pair is formed as an intermediate state that subsequently dissociates into two uncorrelated triplet excitons (**Figure 1A**). Distinct from the independent triplets, the triplet-pair, ^{1}(TT), is a doubly-excited, spin-singlet state composed of two triplets that maintain electronic and spin coherence, making SF a special

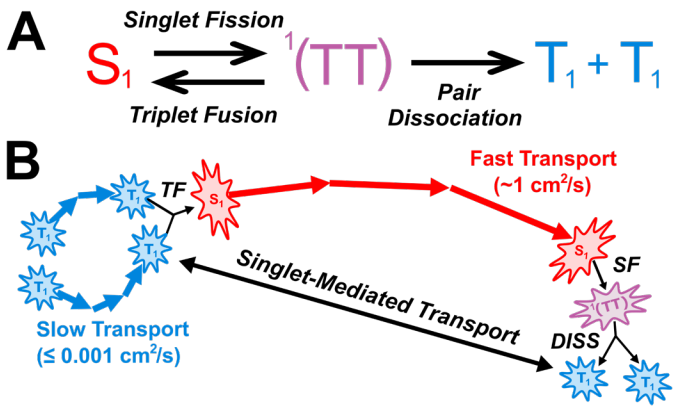

Figure 1: (A) Reaction scheme describing triplet pair, ^{1}(TT), formation via singlet fission followed by either triplet pair dissociation into independent triplets, T_1+T_1, or triplet fusion to reform the singlet state, S_1. (B) The interconversion of singlet and triplet populations via singlet fission and triplet fusion allows for singlet-mediated transport. Abbreviations: TF – triplet fusion; SF – singlet fission; Diss: Pair Dissociation.

case of internal conversion.[36,37] Importantly, the lone singlet exciton can be regenerated through recombination of the two independent triplet excitons or the triplet-pair state. This leads to an equilibrium between the singlet and triplet exciton populations, the composition of which is largely dictated by both molecular electronic structure and packing arrangements in the solid state.[1,38] Most research on SF-materials focuses on optimizing these two design handles to skew the equilibrium toward the formation of independent triplets. In particular, it is widely thought that slightly exoergic or isoergic SF configurations, wherein the lowest spin-singlet state energy is greater than or equal to twice the lowest spin-triplet state energy $E(S_1) \geq 2E(T_1)$, is ideal. While this type of energetic alignment typically results in sub-picosecond SF rates and high triplet yields, little consideration is given to the subsequent, equally important step of exciton transport.

The transport of Frenkel excitons, tightly bound electron-hole pairs in low dielectric materials, is mediated by different mechanisms depending on whether the net spin of the exciton is zero (singlet) or one (triplet). Triplet exciton transport occurs through a Dexter-type electron-exchange coupling[39] that is mediated by wavefunction overlap between neighboring molecules. This dependence on nearest-neighbor coupling makes Dexter transfer highly susceptible to

disruption by structural inhomogeneity within a material. Namely, trap sites that form when the energetic disorder is comparable to the thermal energy (k_BT)[40] and altered molecular packings at defects, grain boundaries,[41–43] and crystal edges[44–46] that induce poor wavefunction overlap between molecules can each act to hinder triplet exciton diffusion. The effect of structural disorder is readily observed in polyacene materials like rubrene where triplet diffusion lengths drop from 2 – 8 μm in highly ordered rubrene crystals[47,48] to 25 – 30 nm in disordered rubrene films.[49] In contrast, spin-singlet exciton transport is often described by the Förster mechanism, which involves an inductive, long-range Coulombic coupling between donor and acceptor transition dipole moments that can make their transport less susceptible to disruption by local disorder. The larger spatial delocalization of singlet excitons with respect to triplet excitons can also boost their transport by enhancing their transition dipole moment.[50–52] As a result, diffusion constants for singlet excitons are typically orders of magnitude larger than those of triplet excitons in organic solids.[53]

While Förster transfer is inaccessible for triplet excitons due to the lack of a transition dipole that links them to the ground spin-singlet state, in systems with a slightly endoergic SF configuration ($\Delta E_{SF} = E(S_1) - 2E(T_1) < 0$), such as rubrene or tetracene,[54] triplet pairs can undergo triplet fusion (TF) to reform a spin-singlet exciton that can rapidly diffuse prior to undergoing SF once again (**Figure 1B**). In this singlet-mediated triplet transport pathway, triplets can exploit the faster transport available to singlet excitons, possibly increasing their effective diffusion length by several tens to hundreds of nanometers. However, this extended diffusion range comes at a potential cost as introducing an endoergic barrier to SF will naturally skew the equilibrium between singlet and triplet excitons towards the singlet state. Developing design principles for optimizing singlet-mediated transport without making significant sacrifices in triplet yield can provide a

means by which the problem of slow triplet exciton transport can be overcome.

Up until now, singlet-mediated transport has only been directly observed in tetracene and rubrene crystals.[47,55–58] However, using these and other acenes in light-harvesting devices introduces some key challenges due to their low photostability in the presence of oxygen[59,60] and relatively low molar extinction coefficients,[61,62] which exacerbate the mismatch between the triplet diffusion length and optical absorption depth. In contrast, perylenedimides (PDIs) constitute a particularly promising family of SF-capable compounds as they are highly resistant to photooxidation[63,64] and possess large molar extinction coefficients on the order of $5-10\times10^{4}\ \mathrm{M^{-1}cm^{-1}}$.[7,65–69] Importantly, several PDIs exhibit an endoergic barrier for SF that is similar to that of tetracene, ΔE_{SF} = – (0.2 – 0.27) eV,[7,67,70,71] yet have demonstrated SF with high triplet yields.[7,71–73] In solids, PDIs form 1D slip-stacked columns[74–78] wherein strong charge transfer coupling between neighboring molecules allows them to undergo efficient SF despite the unfavorable energetic alignment of their singlet and triplet states.[71,79,80]

N,N'-bis(2-phenylethyl)-3,4,9,10-perylenedicarboximide (EP-PDI) is a particularly well-suited chromophore for SF as it exhibits a triplet yield up to 189% in disordered thin films[71] and is predicted to display a SF rate on the picosecond timescale.[79] However, little work has been done to characterize exciton transport in this system. As such, EP-PDI was chosen as the focus of this work wherein we use femtosecond transient absorption microscopy (TAM) to directly image excitons within molecular crystals in space and time and elucidate mechanisms leading to their transport. We find that SF in EP-PDI crystals is accelerated by nearly two orders of magnitude (k_{SF} = 1/3.3 ps^{-1}) relative to rates of triplet pair production reported for EP-PDI thin-films (k_{SF} = 1/260 ps^{-1}) that exhibit substantial structural inhomogeneity on the micron scale.[71] Our TAM measurements also display evidence for the existence of singlet-mediated transport in EP-PDI

crystals that enhances their effective triplet diffusion length by ~205 nm within the first 500 ps after photoexcitation. By using numerical simulations to model exciton diffusion and extract important kinetic parameters that influence singlet-mediated transport, we find it is optimized in SF-materials when the ratio of rate constants for SF and TF (k_{SF}/k_{TF}) is between 1.9 and 3.8. Interestingly, we find small EP-PDI crystals that contain some degree of structural disorder can display SF rates that are slowed by nearly a factor of 4 relative to large EP-PDI crystals. While perhaps counter-intuitive, our modeling suggests this slowing of the SF rate in small crystals moves their k_{SF}/k_{TF} ratio into closer alignment with ideal values for singlet-mediated transport and thereby extends their triplet diffusion lengths. Our findings highlight EP-PDI as a promising candidate SF-material; explicate relationships among structural ordering, the SF process, and singlet-mediated transport in EP-PDI crystals; and point to a set of design principles for enhancing singlet-mediated transport in future SF-materials.

Results and Discussion

Structural Characterization of EP-PDI Single Crystals. Needle-like EP-PDI crystals were grown via a drop-casting method similar to the crystallization procedure outlined in Ref. 81 with slight modifications (**Supporting Information**, Section SI). Notably, we found crystals of visibly different quality and size could be preferentially grown by increasing the temperature of the growing conditions, forming what we designate as α- and β-crystals, respectively. Optical microscopy images show distinct morphological differences between the two crystal types (**Figure 2A**). The α-crystals, which are grown quickly at low temperature, are ~1 – 3 μm in width and ~15 – 50 μm in length and have visible defects that likely originate from kinetically trapped structures formed during rapid crystallization. These defect sites can introduce small structural deviations from the molecular packing arrangement preferred within the crystal's bulk because of relaxed

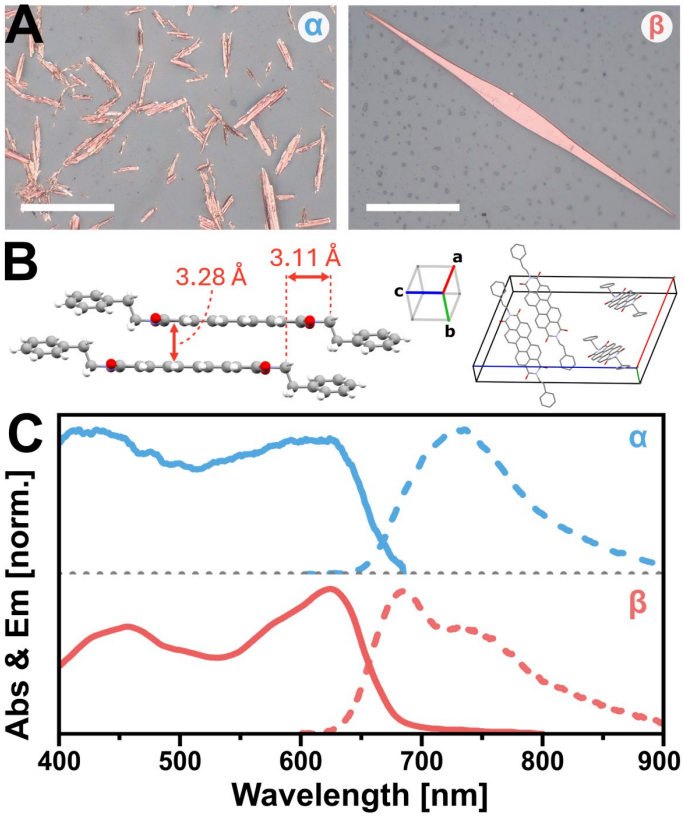

Figure 2: (A) Optical microscopy images of α (left) and β (right) EP-PDI crystals grown via drop-casting a heated EP-PDI toluene solution onto DI-water at 20 °C and 40 °C respectively. The scale bar in both images is 50 μm. (B) Structure of an EP-PDI α-crystal showing its unit cell and slip-stacked packing arrangement of neighboring EP-PDI molecules, with displacements of 3.28 Å along their π-π stacking direction, 3.11 Å along their long (longitudinal) axis, and 0.62 Å along their short (transverse) axis (not shown). The π-π stacking occurs primarily along the crystalline *b*-axis. (C) Absorption and PL spectra of α- and β-crystals collected via absorption and emission microscopy.

structural constraints near interfaces and grain boundaries.[45] In contrast, the β-crystals, which are grown slowly at elevated temperature, are much larger, with widths of ~10 – 15 μm and lengths of ~100 – 200 μm. These crystals also lack visual defects, which indicates their slower growth aids in the optimization of intermolecular interactions that order the crystal's structure and morphology.

Prior work has noted EP-PDI can form at least two distinct crystal structures that differ in their π-π stacking distance and the angle formed between the plane of the PDI core and its pendant phenyl groups.[75,77,78,82] To determine if the different morphologies of the α- and β-crystals stem from them being comprised of distinct polymorphs, we used microcrystal electron diffraction

(MicroED)[83] to determine their underlying crystal structures. MicroED enables the determination of atomically resolved structures using crystals 10^6 times smaller than typically required for x-ray diffraction, and has demonstrated utility for structure determination of organic semiconductors.[84,85] The structures of both α- and β-crystals were solved using data collected at ~90 K from two and four crystals, respectively (**Figure S2**). Both α and β crystallize in the monoclinic space group C2/c and adopt structures that are very similar to one previously reported by Hädicke and Graser.[77,78] **Figure S2** and **Table S1** highlight the notable differences between α, β, and the previously reported structure. Because MicroED necessitates data collection from multiple crystals, we were able to compare the unit cell lengths of multiple α- and β-crystals. The two α-crystals were characterized by having slightly longer unit cell lengths along the crystallographic a-axis and shorter unit cell lengths for the crystallographic b- and c-axes when compared to all four β-crystals. Although these differences appear small, they are statistically distinct and reflect the differences in each microcrystal.

The structure obtained for the α-crystals shows that PDIs are arranged into slip-stacked columns wherein molecules are slipped longitudinally by ~3.11 Å and experience a small transverse displacement of ~0.62 Å (**Figure 2B**). This large longitudinal slip has previously been highlighted to enhance SF by leading to constructive overlap of EP-PDI's HOMO and LUMO orbitals, which increases the electronic couplings involved in charge transfer-mediated SF.[80,86] The short π-π stacking distance between neighboring EP-PDI molecules of ~3.28 Å acts to further strengthen these couplings. For β-crystals, the longitudinal and transverse slips are found to be ~3.15 Å and ~0.51 Å, respectively, while the π-π stacking distance adopts a value of ~3.30 Å. These slight differences likely result from variations in the internal strain of α- and β-crystals due to their differing size.

To determine the impact of these differences on SF, we used a dimer model to compute the electronic couplings involved in SF (**Supporting Information**, Section SIII). These calculations employ a formalism outlined by Berkelbach et al. that accounts for both for direct two-electron coupling between the S_1 and ^{1}(TT) states as well as coupling between these states mediated by charge transfer pathways.[87] We find that the magnitude of the effective SF coupling is roughly 4.4× larger for β-crystals relative to α-crystals, which per Fermi's Golden Rule would predict that SF should be nearly 20× faster in β-crystals. This finding highlights that subtle changes in crystal structure can have a large impact on SF, which is consistent with prior work on PDI[71,80,88] and diphenylisobenzofuran solids.[89,90]

Optical absorption and photoluminescence (PL) microscopy further highlight differences in the electronic properties of α- and β-crystals (**Figure 2C**). The absorption spectra of both crystal types consist of two prominent absorption bands centered at ~630 and ~450 nm that span most of the visible region and bear a strong resemblance to the "black phase" spectrum observed in thermally annealed EP-PDI films.[73,82] The large bandwidth of these spectra arises from two interfering contributions to the excitonic coupling between molecules within each crystal,[71,91–94] a coulombic H-type coupling, which stems from the interaction of transition dipole moments on nearby molecules, and an opposing charge transfer J-type coupling that arises due to orbital overlap of the frontier molecular orbitals of neighboring molecules. Since the π-stacking is relatively close in the EP-PDI crystals, the strength of the charge transfer coupling dominates in EP-PDI, leading to an overall red-shift in its absorption onset relative to isolated EP-PDI molecules in solution.

Comparing absorption spectra of the two crystal types, we find the α-crystal spectrum exhibits a considerable degree of peak broadening relative to that of the β-crystal. This inhomogeneous broadening is suggestive of structural disorder and implies α-crystals contain a

larger degree of internal structural variation relative to β-crystals. Differences are also found in the PL spectra of the two crystals and may be associated with their degree of structural disorder. In the β-spectrum, we observe emission peaks that largely mirror the crystals' low-energy absorption band, indicating that excimer formation does not occur within the crystal. On the other hand, the α-spectrum closely resembles the PL spectrum of disordered EP-PDI thin films[71] and appears to be both broadened and red-shifted relative to the β-spectrum. A red-shifted PL spectrum can arise from downhill exciton migration to lower energy sites in the crystal, which should be more pronounced in systems with a larger degree of structural and energetic variation.[57,95–97]

Exciton Transport in EP-PDI Crystals. Next, we set out to directly measure exciton transport in both α- and β-crystals using a homebuilt femtosecond transient absorption microscope (TAM) configured for galvo-scanning measurements.[98] Here, a 530 nm pump beam was focused onto an EP-PDI crystal while galvo mirrors raster-scanned a focused 650 nm probe beam across a 4×4 μm size area, resulting in a transient absorption image that represents the spatial distribution of excitons within the crystal at a particular pump-probe time delay. **Figure 3A** highlights some of these measurements performed on an α-crystal at four different time delays, showing snapshots of the exciton distribution 0, 15, 250, and 800 ps after photoexcitation by the pump. Similar measurements collected for a β-crystal are shown in Section SVI of the **Supporting Information**. The positive signal measured at this probe wavelength corresponds to a ground state bleach (GSB) associated with photoexcited EP-PDI molecules. While such a signal in principle should show equal contributions from singlet and triplet excitons, prior work has shown that the EP-PDI GSB is partially cancelled by an overlapping triplet induced absorption band, which makes this signal more sensitive to the singlet exciton population.[71] As the singlet and triplet excitons diffuse through the crystal, the measured signal distribution will evolve, providing a direct measure of

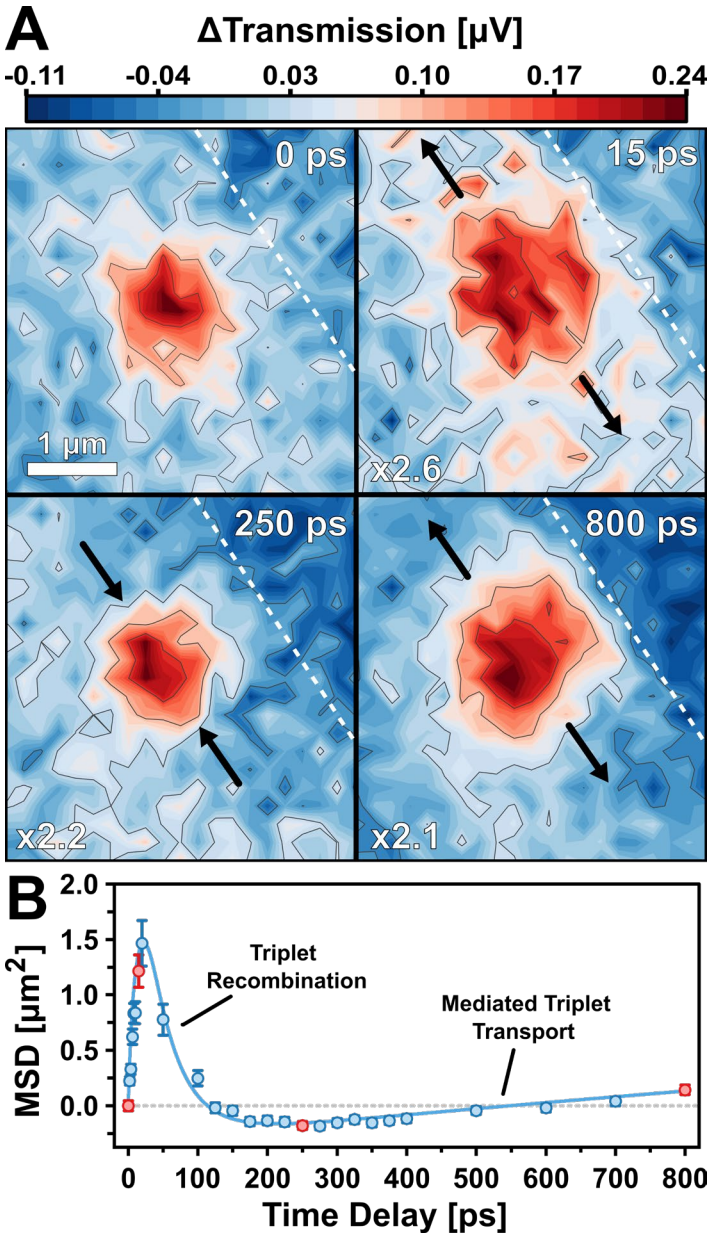

Figure 3: (A) Scaled TAM galvo-scanning measurements performed on an α-crystal showing the spatially varying transient absorption signal at 0, 15, 250, and 800 ps after excitation. A dashed white line marks the edge of the α-crystal and black arrows indicate the spatial time evolution of the signal distribution. (B) Plot of the experimentally measured (circles) and numerically simulated MSD (solid blue curve) of the TAM signal as a function of pump-probe time delay. Red data points correspond to the measurements highlighted in the images in (A).

exciton transport.

In a TAM experiment, the focused pump beam generates an initial distribution of excitons, $n(x, y, 0)$, whose spatial arrangement reflects the size and shape of the pump point-spread

function, which can be approximated as a two-dimensional (2D) Gaussian with an initial variance of $\sigma^2(0)$:

$$n(x, y, 0) = N * exp\left[-0.5\left(\frac{(x - x_0)^2 + (y - y_0)^2}{\sigma^2(0)}\right)\right] \quad [1]$$

Spatial diffusion of the exciton population over time will preserve the Gaussian shape, allowing us to extract the time-dependent variance, given as $\sigma^2(t) = 4Dt + \sigma^2(0)$ for 2D diffusion, using the following equation:

$$n(x, y, t) = N * exp\left[-0.5\left(\frac{(x - x_0)^2 + (y - y_0)^2}{4Dt + \sigma^2(0)}\right)\right] \quad [2]$$

Here, D is the exciton diffusion coefficient that is directly related to the mean squared displacement (MSD = $4Dt$).[57,99,100]

The time-dependent MSD of the TAM signal for an α-crystal is highlighted in **Figure 3B**. In a normal diffusive regime, the MSD is expected to grow monotonically and linearly with time. However, we observe an anomalous evolution of the MSD curve as its value increases rapidly in the first 15 – 20 ps due to a combination of singlet-singlet exciton annihilation and exciton diffusion. Following this growth, the MSD shrinks, reaching a minimum size by 250 ps. Interestingly, the FWHM of the TAM signal at 250 ps is ~440 nm narrower than the initial value generated by the pump. The MSD then continues to grow monotonically and linearly over time delays longer than 250 ps.

This behavior is qualitatively similar to measurements reported by Berghuis *et al.* that examined tetracene crystals using PL microscopy, which selectively monitors the singlet exciton population.[58] There, the anomalous shrinking of the singlet exciton distribution was attributed to TF, which can regenerate singlet excitons following SF. As this process can exhibit a quadratic

dependence on the triplet exciton population, TF selectively occurs within the center of the exciton distribution generated by the pump, thereby causing the FWHM of the signal to shrink over time. Given that the GSB we observe selectively probes the singlet exciton population, we hypothesize that TF underlies the anomalous shrinking of the EP-PDI TAM signal shown in **Figure 3B**. However, a key point of difference between behavior reported in tetracene crystals[58] and the measurements we report for EP-PDI crystals is the timescale over which the anomalous behavior occurs. In tetracene crystals, shrinking of the singlet exciton distribution due to TF occurs over the course of several nanoseconds whereas in EP-PDI crystals, shrinking occurs within the first 100 – 200 ps following photoexcitation, depending on the crystal. We note that if the anomalous behavior stems from TF, then the generation of triplet excitons via SF must have already occurred prior to shrinking of the singlet exciton distribution. Thus, the difference in timescales must arise from a difference in SF rates between tetracene and EP-PDI. Importantly, this implies that the overall shape of the MSD curve (i.e., the spatial evolution of the singlet excitons) not only carries information about exciton diffusion rates but also kinetic information relating to SF and TF.

Numerical Simulations of Exciton Diffusion. To test if our assignment of the evolution of the MSD curve is consistent with dynamics stemming from SF and TF, we fit our TAM data using an exciton diffusion simulation that accounts for the interconversion of singlet and triplet exciton populations. Our three-state kinetic model begins with an initial singlet exciton population that either relaxes to the ground state (k_{SD}) or undergoes SF (k_{SF}), forming a triplet pair state that can dissociate (k_{dis}) into independent triplet excitons. The singlet and triplet populations are coupled through both geminate and non-geminate recombination pathways. Geminate recombination occurs when the triplet pair state undergoes TF to reform the singlet exciton (k_{TF}^{G}) and has a linear dependence on the triplet pair population density. In contrast, non-geminate

recombination involves two uncorrelated triplet excitons annihilating (k_{TF}^{NG}) and is quadratically dependent on the triplet population density.

The spatial evolution of the signal intensity can be modeled by the following three coupled partial differential equations:

$$\frac{\partial n_S}{\partial t} = D_S \nabla^2 n_S - k_{SD} n_S - k_{SF} n_S - k_{SSA} n_S^2 + k_{TF}^{G} n_{TP} + k_{TF}^{NG} n_T^2 \quad [3a]$$

$$\frac{\partial n_{TP}}{\partial t} = -k_{TPD} n_{TP} + k_{SF} n_S - k_{TF}^{G} n_{TP} - k_{dis} n_{TP} \quad [3b]$$

$$\frac{\partial n_T}{\partial t} = D_T \nabla^2 n_T - k_{TD} n_T + 2(k_{dis} n_{TP} - k_{TF}^{NG} n_T^2) \quad [3c]$$

where n_S, n_{TP}, and n_T respectively represent the spatial distributions of singlet excitons (S_1), triplet pairs (^{1}(TT)), and triplet excitons (T_1). The factor of 2 in front of the dissociation and non-geminate TF rate terms in Eq. 3c represents the generation of two triplet excitons as the result of triplet pair dissociation and the removal of pairs of triplet excitons through bimolecular annihilation. We emphasize that this is a minimal model for describing the exciton dynamics occurring after excitation. Removal of any component of the model, such as the presence of a distinct triplet pair population, n_{TP}, or either the geminate (k_{TF}^{G}) or non-geminate (k_{TF}^{NG}) triplet fusion pathway, prevents us from producing acceptable fits to our data (**Supporting Information**, Section SV).

These coupled equations cannot be solved analytically so we instead integrated them numerically at discrete time points using a Crank-Nicolson algorithm[101] to approximate the spatial and time derivatives. We note that while intrinsic diffusion constants D_S and D_T are assigned to the singlet and triplet exciton populations, respectively, only the singlet excitons are mobile in these simulations as it is unlikely that the triplets will diffuse to an appreciable extent via Dexter energy transfer within the 800 ps window we probe during our measurements. We therefore

decided to keep D_T fixed at 0 as changing it by multiple orders of magnitude did not significantly affect the fitting results, preventing us from determining an accurate value of D_T. In most TAM measurements, due to the tightly focused laser pulses, singlet excitons are produced at excitation densities wherein singlet-singlet exciton annihilation (SSA) is unavoidable, making it necessary to explicitly consider it when modeling TAM data. To account for SSA, we simultaneously fit three data sets recorded for each crystal type using different initial exciton densities (**Figures 5A** and **S6**) to determine the SSA rate (k_{SSA}).

The solid lines shown in **Figures 3B, 5A, 6A,** and **S6** represent fits produced by this model to experimental MSD curves for α- and β-crystals. We find the model well reproduces the experimental data, capturing both the anomalous shrinking behavior as well as exciton density dependence and thereby allows us to better understand the physical processes occurring in the crystal after photoexcitation. As predicted, we found the shape of the MSD curves to be highly sensitive to the rates of SF and TF, providing a means for correlating SF kinetics with the distinct transport properties of individual EP-PDI crystals. The resulting fitting parameters for α- and β-crystals are summarized in **Table 1**. We find that the SF rate in β-crystals (1/3.3 ps^{-1}) is approximately four times faster than the rate determined for α-crystals (1/14 ps^{-1}). This result is qualitatively consistent with our calculations of the SF couplings for α- and β-crystals, which predict that SF should be nearly 20× faster in β-crystals. The difference we observe between the computed ratio of SF rates for α- and β-crystals and our experimentally determined one may stem from a lack of a full treatment of vibronic coupling in our calculations, which has been shown to impact SF in PDI crystals.[79] Importantly, the SF rate we obtain for β-crystals is over an order of magnitude faster than its corresponding value reported for EP-PDI thin films (1/260 ps^{-1}).[71] Slower SF rates for PDI thin films vs. crystals has previously been noted.[102] We hypothesize that the

Table 1: Fitting parameters used to model exciton transport in EP-PDI Crystals.

Rate Constant	α-crystal	β-crystal	Meaning
$1/k_{SD}\ [ps]$	4100	4100	Decay rate of singlet excitons[a]
$1/k_{TD}\ [ps]$	0	0	Decay rate of triplet excitons[b]
$1/k_{TPD}\ [ps]$	0	0	Triplet pair decay rate[b]
$1/k_{SF}\ [ps]$	14 ± 2.3	3.3 ± 0.8	Singlet fission rate
$1/k_{TF}^{G}\ [ps]$	180 ± 30	330 ± 135	Geminate triplet fusion rate
$1/k_{dis}\ [ps]$	100 ± 17	140 ± 55	Triplet pair dissociation rate
$k_{SSA}\ [\mu m^3/ps]$	1.6×10^{-11}	1.3×10^{-10}	Singlet-Singlet annihilation rate
$k_{TF}^{NG}\ [\mu m^3/ps]$	6.1×10^{-13}	3.6×10^{-12}	Non-Geminate triplet fusion rate
$D_S\ [\mu m^2/ps]$	$8 \pm 3 \times 10^{-4}$	$20 \pm 15 \times 10^{-4}$	Singlet exciton diffusion constant
$D_T\ [\mu m^2/ps]$	0	0	Triplet exciton diffusion constant[b]

[a]The decay rate of singlets, k_{SD}, was fixed using the value from Ref [71].
[b]The triplet pair decay rate, k_{TPD}, triplet decay rate, k_{TD}, and the triplet diffusion constant, D_T, were fixed at 0 due to the limited time window of the experiment (~1 ns).

slower SF rate observed for EP-PDI thin films vs. β-crystals arises from the inclusion of grain boundaries in thin films that likely act to hinder SF.

To examine the exciton dynamics occurring in EP-PDI crystals that lead to the anomalous shrinking behavior in more detail, we separated out the total singlet exciton density into prompt and delayed singlet populations (**Supporting Information**, Section SV). Prompt singlets are those that were initially generated by the pump pulse while delayed singlets are those regenerated through geminate and non-geminate TF (**Figure 4A**). Tracking the width of the prompt, delayed, and total singlet exciton distributions in the simulation shows that the shrinking of the total singlet distribution is accompanied by the generation of delayed singlets with a narrower spatial distribution than the initial distribution of the prompt singlets (**Figure S5B**). Because there are two pathways by which delayed singlets can be generated, we simulated scenarios where either geminate or nongeminate TF was turned off to parse out their roles in delayed singlet generation (**Figure S4**). For nongeminate TF, its quadratic population dependence causes it to occur more efficiently near the center of the triplet exciton distribution, where the highest density of excitons

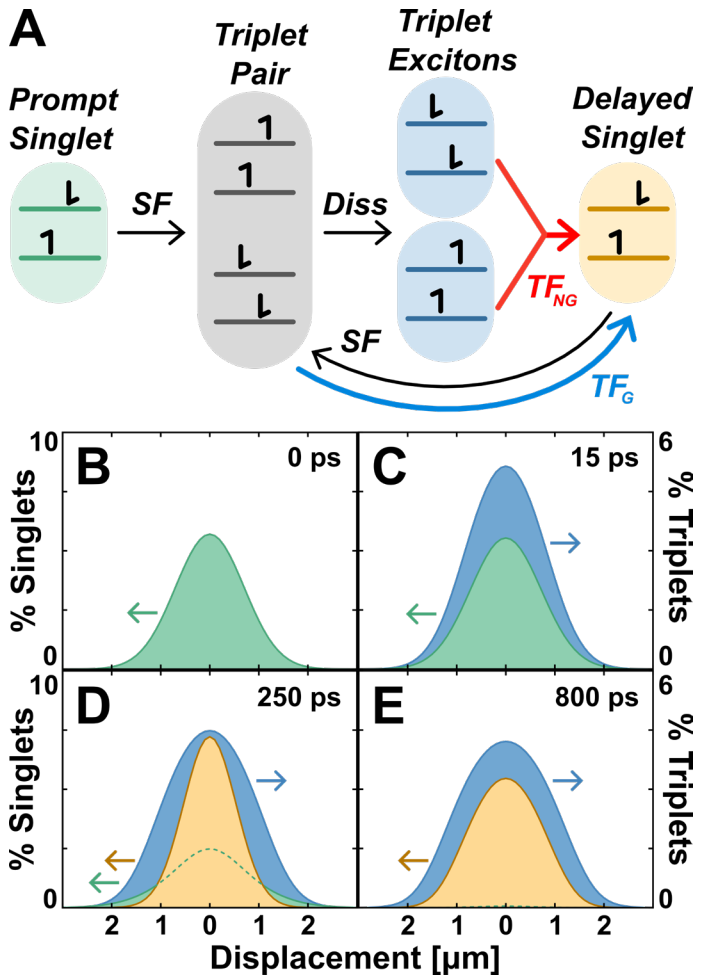

Figure 4: (A) Modified kinetic model for simulating the evolution of prompt singlets initially generated by the pump pulse and delayed singlets formed through geminate (TF_G) and non-geminate TF (TF_{NG}). (B–E) Profile slices of the simulated prompt singlet (green), triplet (blue), and delayed singlet (yellow) exciton distributions at four time points matching those highlighted in **Figure 3A**. Scales on the y-axes show the percentage of the total singlet (left) and total triplet (right) populations.

is located, and thus produces more delayed singlets there than at the edges of the distribution. This increases the measured TAM signal toward the center of the pump focal spot, leading to its spatial narrowing over time. Likewise, geminate TF leads to a spatial narrowing of the TAM signal due to the immobility of triplet excitons, including triplet pairs, in our model. Triplet pair formation halts exciton migration, thus when delayed singlets are generated via geminate TF, they possess a narrower spatial distribution than that of prompt singlets that continue to diffuse over time.

To visualize how the different exciton populations evolve with time within EP-PDI

crystals, we took profile slices of the simulated exciton distributions at each time point. The panels in **Figures 4B - 4E** show four of these profile slices at time points that match the experimental TAM maps highlighted in **Figure 3A** for the α-crystal. At time zero, we see a distribution of prompt singlets (green area in **Figure 4B**) that represent the excitons generated by the pump pulse. As expected, given the fast SF rate in the α-crystal, a large triplet population forms within 15 ps (blue area in **Figure 4C**). As TF starts to occur, delayed singlets begin to form (yellow in **Figure 4D**) and by 250 ps the delayed singlets occupy a noticeably narrower spatial distribution than the prompt singlets. Interestingly, comparing the simulated exciton distributions at 250 ps with those at 800 ps (**Figure 4E**), we find that the triplet distribution broadens coincidently with the delayed singlet distribution despite triplets being immobile in the simulation ($D_T = 0$). Experimentally, this time range corresponds to one wherein the exciton MSD grows linearly with time, suggesting normal diffusive behavior, which we assign to the diffusion of delayed singlets based on our model. Because the delayed singlets are formed from the recombination of triplets, the correlation in the simulations between spreading of the triplet and delayed singlet populations shows that interchange between singlets and triplets via SF and TF acts to accelerate triplet diffusion within EP-PDI crystals.

To verify this conclusion experimentally, we performed TAM measurements at different pump fluences to observe how exciton transport at long time delays was impacted. Because the rate of non-geminate TF depends on exciton density, we expect more delayed singlets to be generated at higher fluences and thereby enhance singlet-mediated transport. This is indeed what we observe in **Figure 5A**, which shows a stacked plot of three TAM diffusion measurements performed on an α-crystal at different exciton densities. As the exciton density increases, two noteworthy changes in the MSD curve arise: First, the initial rise of the MSD at early times

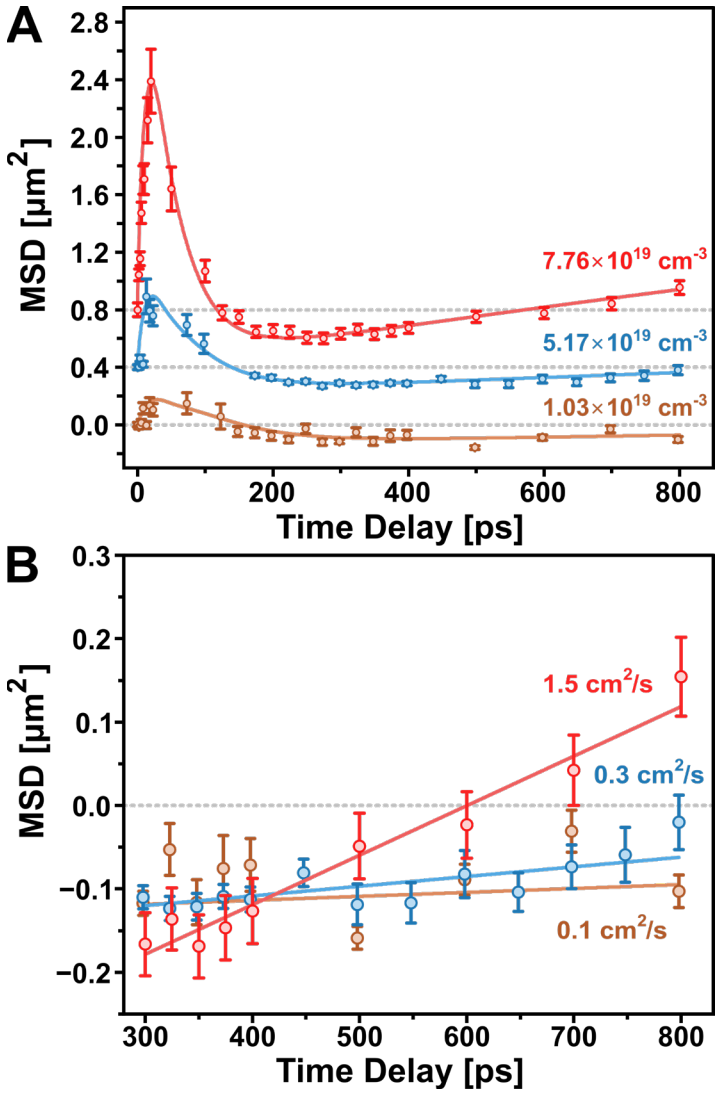

Figure 5: (A) MSD curves from three TAM diffusion measurements performed on an α-crystal with varying excitation densities. The data are offset for clarity and gray dashed lines show the zero-point for each dataset. (B) Zoom in of the MSD curves at delays of 300 – 800 ps that highlight an increase in the MSD slope with increasing excitation density.

becomes increasingly exaggerated due to an increased efficiency of SSA, which selectively depletes excitons near the center of the exciton distribution.[58] Second, over time delays of 300 – 800 ps, we see an increase in the slope of the MSD curve, with values ranging from 0.12 to 1.49 cm^2/s for the low and high fluence measurements respectively (**Figure 5B**). In comparison to other reported triplet diffusion constants,[53] these values are orders of magnitude faster than expected and are unlikely to reflect the intrinsic triplet diffusion rate in EP-PDI. They are also markedly slower

than what is typical for singlet excitons in organic crystals,[53] suggesting that these values do not represent the intrinsic singlet diffusion rate either. Indeed, prior studies examining exciton diffusion in disordered EP-PDI films have suggested singlet diffusion rates that are at least as fast as 7 cm^2/s.[103,104] This is consistent with our model, which can reproduce the curves in **Figure 5A** using a singlet diffusion constant of 8 cm^2/s, a value that is an order of magnitude larger than the diffusion constants inferred by linearly fitting the data in **Figure 5B**. Thus, we conclude that these diffusion rates represent an effective diffusion constant, D_{eff}, whose value represents the combined diffusion of the exchanging singlet and triplet population. As triplets diffuse slowly, the value of D_{eff} is reduced relative to that of singlet excitons. However, by skewing the equilibrium between singlets and triplets towards the singlet state, as is accomplished in **Figure 5B** by increasing exciton density to favor TF, D_{eff} can be increased.

Comparing Exciton Transport Within α- and β-Crystals. To determine how slight structural variations within EP-PDI crystals impacts singlet-mediated exciton diffusion, we also preformed TAM diffusion measurements on a β-crystal at three different pump fluences (**Figure S6**). In these measurements, we see the same behavior that was observed in α-crystals where the MSD grows, shrinks, and then grows again; however, it occurs over an appreciably shorter timescale in β-crystals (**Figure 6A**). This difference in timescales is partly due to the higher value of k_{SF} in the β-crystal as this influences how rapidly independent triplet excitons appear that subsequently generate delayed singlets, thereby modulating the MSD of the TAM signal. By extension, the difference in timescales also indicates a difference in their singlet-mediated triplet transport capabilities. This is most obviously seen in **Figure 6B** where the later time delays are highlighted and show an approximately three-fold enhancement of D_{eff} in the β-crystal compared to the α-crystal.

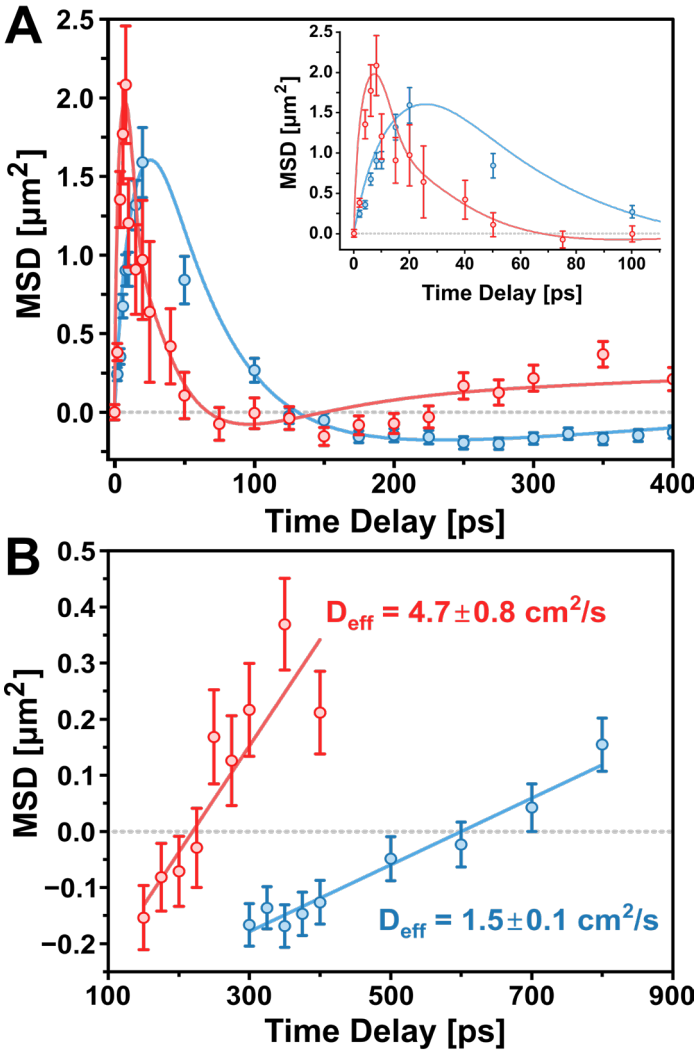

Figure 6: (A) Comparison of MSD curves for the α-crystal (blue) and β-crystal (red). The inset shows a zoomed in view of the transport dynamics occurring within the first 100 ps after excitation, and solid curves show the fits from our numerical simulation. (B) MSD curves at later times delays showing the difference in the effective triplet diffusion constant, D_{eff}, for the α- and β-crystals.

To rationalize this enhancement in D_{eff}, we first considered the rates of nongeminate TF for both crystals. For the α-and β-crystals respectively, the nongeminate TF rates were 6.1×10^{-13} μm^3/ps and 3.6×10^{-12} μm^3/ps, which follow the same trend as D_{eff}, consistent with what would be expected for enhanced singlet-mediated transport in the β-crystal. A similar trend is also seen among tetracene, rubrene, and TIPS-pentacene in which tetracene, having the most significant singlet-mediated contribution to triplet transport out of the three, has the fastest rate of singlet

regeneration by nongeminate TF.[54] The rate of bimolecular exciton annihilation, however, only provides a partial explanation for the enhanced D_{eff} as other exciton dynamics also play a significant role.

To improve D_{eff}, the rates of both singlet regeneration and singlet exciton transport need to be optimized. To the former point, comparing D_S between the two EP-PDI crystals studied here ($D_S^{\alpha} = 8$ cm^2/s and $D_S^{\beta} = 20$ cm^2/s), reveals another trend consistent with enhanced singlet-mediated transport in the β-crystal. Faster singlet diffusion in β-crystals is expected based on our steady-state spectroscopic measurements (**Figure 2**), which show that β-crystals exhibit ~1.65× larger overlap between their absorption and PL spectra relative to the α-crystals. According to Förster energy transport theory,[105,106] increasing this spectral overlap will accelerate the rate of singlet energy transfer between different sites within a crystal. Moreover, the higher degree of structural disorder within α-crystals inferred from the broadening of its absorption and PL lineshapes relative to β-crystals may also have a negative impact on singlet transport by lowering the orientational factor in Förster theory whose value is dependent on the relative alignment of transition dipole moments on donor and acceptor molecules. Structural defects that lead to a distribution of molecular alignments across a crystal will act to lower D_S, which likely occurs to some degree within α-crystals.

Simulating Exciton Transport at Solar Fluence. Non-geminate TF is only expected to have a significant impact on singlet regeneration at exciton densities above the annihilation threshold of the material. This threshold is typically higher than 1×10^{13} cm^{-3} for organic solids making it several orders of magnitude higher than the typical exciton density generated by solar flux. Moreover, bimolecular exciton annihilation is diffusion-limited due to the distance dependence of the excitonic interactions that facilitate the process; that is, either by a collisional

interaction such as with Dexter energy transfer or by a columbic interaction where one exciton migrates within the Förster-radius of another exciton. A slower rate of triplet exciton transport, therefore, translates into a lower probability of encounters between two excitons within their lifetimes and thus acts as a rate-limiting step. As such, relying on slow-moving triplet excitons to undergo non-geminate recombination to access singlet-mediated transport is not likely to improve D_{eff} under low light illumination conditions. Rather, at low light flux, geminate TF will be the primary mechanism by which singlet excitons are regenerated and should be the focus for improving D_{eff}.

To better understand how D_{eff} is influenced under low flux conditions, we simulated exciton diffusion dynamics using an initial singlet exciton population density comparable to what would be generated under solar illumination within EP-PDI. During the first 500 ps of these simulations, we see a maximum effective triplet transport length of ~247 nm using the α-crystal parameters and ~205 nm using the β-crystal parameters (**Figure 7A**). Surprisingly, the α-crystal is predicted to have a ~20% improvement in its effective triplet transport length despite exhibiting more structural disorder, which is often viewed as detrimental to exciton transport. This result is ostensibly in contradiction with our experimental results showing a faster D_{eff} for the β-crystal. However, at lower fluences than those employed in the experimental measurements, we expect geminate TF to make a greater contribution to triplet transport than non-geminate TF. Numerical modeling shows the geminate TF rate for the α-crystal to be nearly twice that of the β-crystal, suggesting that at lower fluences, the α-crystal can more readily access singlet-mediated transport.

This conclusion prompted us to consider how other kinetic parameters in our model can influence singlet-mediated transport. Excluding other population loss pathways, the ratio of SF and geminate TF rate constants, $\kappa = k_{SF}/k_{TF}^{G}$, nominally establishes the equilibrium between the

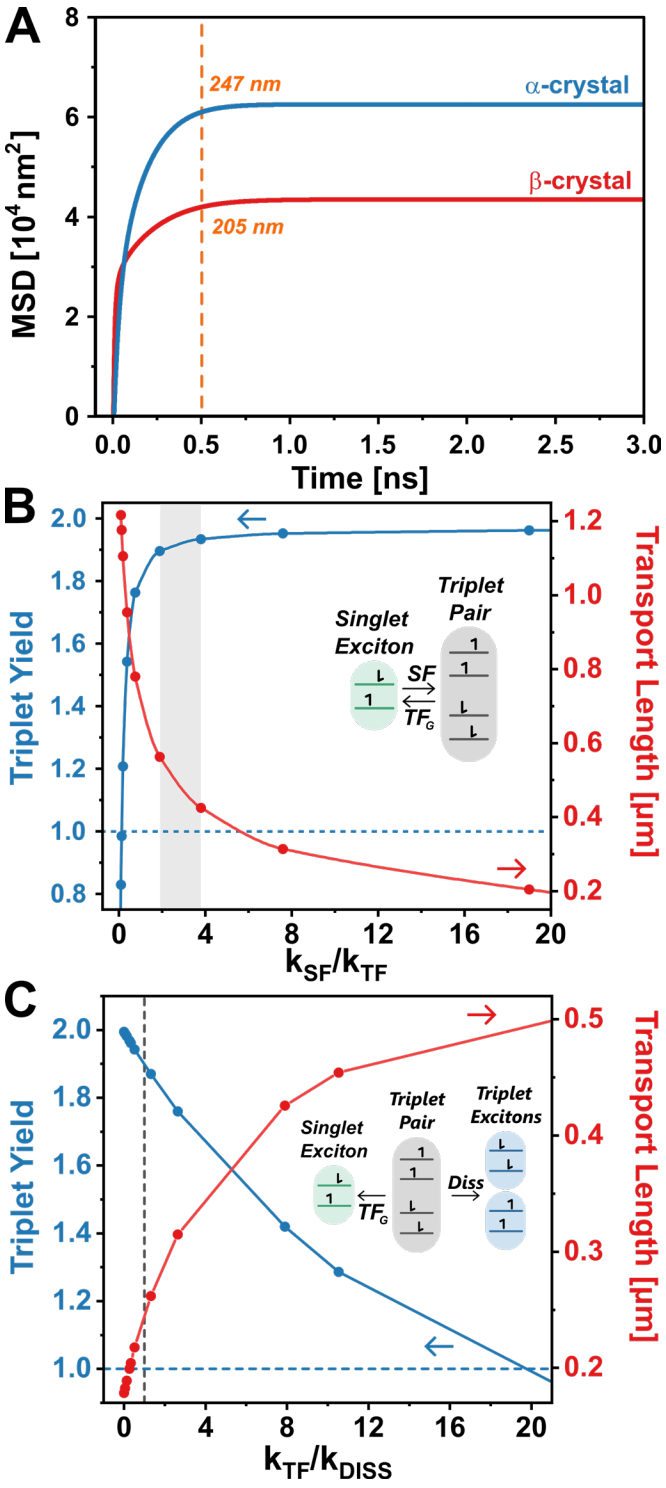

Figure 7: (A) Simulated triplet MSD under solar illumination conditions using the α- and β-crystal parameters. A dashed line indicates the effective triplet transport length 500 ps after photoexciation. (B & C) The effective triplet transport length (right axis) and corresponding triplet yield (left axis) simulated using the kinetic parameters of the α-crystal, varying either (B) κ or (C) γ under solar illumination. The horizontal blue dashed line indicates the half-maximum triplet yield of 100%. In B, the gray block indicates the range of κ ratios between 1.9 and 3.8 while in C, a vertical dashed line indicates where $\gamma = 1$.

singlet and triplet pair populations and thus should have a significant impact on singlet-mediated transport. Indeed, the maximum effective transport length simulated by Zhu, *et al.* for rubrene and tetracene is shorter for rubrene (150 nm, κ = 17.2) but farther for tetracene (260 nm, κ = 8.3), suggesting that a smaller κ value leads to improved transport.[54] Inspired by this, we calculated the maximum triplet transport length and the corresponding triplet yield for varying κ ratios while keeping all other α-crystal kinetic parameters fixed (**Figure 7B**). Here, the triplet yield is determined from the integrated triplet population at the time point in which the transport length is maximized and is normalized by the initial population of singlets at the beginning of the simulation. The resulting plot shows that when singlet-mediated transport is improved, the percent yield of independent triplet excitons decreases, creating a trade-off between SF efficiency and energy transport. The range of κ values between 1.9 and 3.8, however, allow for an optimized transport length of 425 – 563 nm with only a minimal 7 – 10% cost to triplet yield.

The timescale over which the singlet-mediated transport pathway is active is effectively determined by the dissociation rate constant, k_{diss}, of the triplet pair. Thus, we further examined how the maximum triplet transport length and triplet yield vary as a function of the branching ratio $\gamma = k_{TF}^{G}/k_{diss}$, which represents the probability of the triplet pair reforming a singlet exciton instead of dissociating.[1,107] In **Figure 7C**, we plot simulation results computed using a fixed value of κ = 12.9, which corresponds to the κ value of EP-PDI α-crystals. We again find an opposing trend between the maximum triplet transport length and triplet yield. We identify an optimal branching ratio just past γ = 1, shown by the dashed grey line in **Figure 6C**.

Comparing the κ and γ ratios for α-crystals (κ_α = 12.9, γ_α = 0.55) and β-crystals (κ_β = 100, γ_β = 0.42), we see in both cases that the α-crystal has the more optimal ratios for singlet-mediated transport. In the first case, the faster SF dynamics in the β-crystal ($\kappa_\beta > \kappa_\alpha$), which is reflected in

its faster SF rate and slower TF rate, reduces the accessibility of the singlet-mediated transport pathway. In the second case, the higher likelihood for triplet pair dissociation in the β-crystal ($\gamma_\beta < \gamma_\alpha$) serves as a hinderance to singlet-mediated transport by shortening the timescale over which this pathway is active. Thus, while slow SF is often perceived to be detrimental to the performance of SF materials, we find moderately slowing SF can be of great benefit to energy transport. Moreover, we find that very small differences in the structure between α- and β-crystals is responsible for a ~20% difference in triplet exciton transport length. This suggests that subtle tuning of the crystal structure of SF materials can result in a marked difference in their exciton transport ability. We emphasize that structural tuning to optimize parameters such as κ and γ must be done with care to assess the impact of disorder on the intrinsic singlet exciton diffusion rate as a slow singlet diffusion rate can reduce benefits gained from singlet-mediated transport.

Summary & Conclusions

EP-PDI is a promising SF material for light-harvesting applications due to its good photostability, strong light absorption strength and broad absorption spectrum, and its singlet-mediated triplet transport capabilities. However, while allowing for a significant effective triplet transport length, singlet-mediated transport in EP-PDI β-crystals is far from optimized despite their high degree of structural order. On the other hand, while α-crystals show a slower SF rate due to slight changes in their crystal structure and increased internal structural disorder, this slowed rate is closer to an ideal value for enhancing singlet-mediated transport. Although counter-intuitive, we find that altering the structure of a SF-material to slow both its SF rate and rate of triplet pair dissociation can be preferential for triplet exciton transport so long as these structural changes do not also diminish its singlet diffusion. Our findings suggest that optimizing the singlet-mediated triplet transport pathway in future SF-materials will necessitate a fine-tuning of molecular ordering

to confine the k_{SF}/k_{TF}^{G} ratio to be in the range of 1.9 to 3.8 while also keeping the triplet pair branching ratio, γ, slightly greater than 1, marginally favoring the backward reaction as defined in a simple three-state SF model. These two constraints can allow for a triplet transport length on the order of 100's of nanometers while only minimally sacrificing 7 – 10% in triplet yield.

Acknowledgements

This work was supported by the W. M. Keck Foundation under Grant 22605. TSV and BCL acknowledge support from the Center for Adopting Flaws as Features, a NSF Center for Chemical Innovation supported by Grant CHE-2124983. STR and MJR also acknowledge support from the Robert A. Welch Foundation under Grants F-1885 and F-1822, respectively. This work utilized the Alpine high performance computing resource at the University of Colorado Boulder. Alpine is jointly funded by the University of Colorado Boulder, the University of Colorado Anschutz, and Colorado State University.

Supporting Information Available

Procedures for crystal growth and characterization via microcrystal electron diffraction, absorption and photoluminescence microscopy, and TAM; Structures for EP-PDI α- and β-crystals; Calculation of SF couplings for α- and β-crystals; Statistical analysis of noise within TAM images; Description of the numerical exciton diffusion model used to fit TAM data; TAM images highlighting exciton transport in β-crystals; Modeling of exciton transport under solar illumination conditions.

References

(1) Smith, M. B.; Michl, J. Singlet Fission. *Chem. Rev.* **2010**, *110* (11), 6891–6936.

(2) Xia, J.; Sanders, S. N.; Cheng, W.; Low, J. Z.; Liu, J.; Campos, L. M.; Sun, T. Singlet Fission: Progress and Prospects in Solar Cells. *Adv. Mater.* **2017**, *29* (20), 1601652.

(3) Korovina, N. V.; Pompetti, N. F.; Johnson, J. C. Lessons from Intramolecular Singlet Fission with Covalently Bound Chromophores. *J. Chem. Phys.* **2020**, *152* (4), 040904.

(4) Roberts, S. T.; McAnally, R. E.; Mastron, J. N.; Webber, D. H.; Whited, M. T.; Brutchey, R. L.; Thompson, M. E.; Bradforth, S. E. Efficient Singlet Fission Discovered in a Disordered Acene Film. *J. Am. Chem. Soc.* **2012**, *134* (14), 6388–6400.

(5) Burdett, J. J.; Müller, A. M.; Gosztola, D.; Bardeen, C. J. Excited State Dynamics in Solid and Monomeric Tetracene: The Roles of Superradiance and Exciton Fission. *J. Chem. Phys.* **2010**, *133* (14), 144506.

(6) Johnson, J. C.; Nozik, A. J.; Michl, J. High Triplet Yield from Singlet Fission in a Thin Film of 1,3-Diphenylisobenzofuran. *J. Am. Chem. Soc.* **2010**, *132* (46), 16302–16303.

(7) Eaton, S. W.; Shoer, L. E.; Karlen, S. D.; Dyar, S. M.; Margulies, E. A.; Veldkamp, B. S.; Ramanan, C.; Hartzler, D. A.; Savikhin, S.; Marks, T. J.; Wasielewski, M. R. Singlet Exciton Fission in Polycrystalline Thin Films of a Slip-Stacked Perylenediimide. *J. Am. Chem. Soc.* **2013**, *135* (39), 14701–14712.

(8) Lukman, S.; Richter, J. M.; Yang, L.; Hu, P.; Wu, J.; Greenham, N. C.; Musser, A. J. Efficient Singlet Fission and Triplet-Pair Emission in a Family of Zethrene Diradicaloids. *J. Am. Chem. Soc.* **2017**, *139* (50), 18376–18385.

(9) Hartnett, P. E.; Margulies, E. A.; Mauck, C. M.; Miller, S. A.; Wu, Y.; Wu, Y.-L.; Marks, T. J.; Wasielewski, M. R. Effects of Crystal Morphology on Singlet Exciton Fission in Diketopyrrolopyrrole Thin Films. *J. Phys. Chem. B* **2016**, *120* (7), 1357–1366.

(10) Wilson, M. W. B.; Rao, A.; Clark, J.; Kumar, R. S. S.; Brida, D.; Cerullo, G.; Friend, R. H. Ultrafast Dynamics of Exciton Fission in Polycrystalline Pentacene. *J. Am. Chem. Soc.* **2011**, *133* (31), 11830–11833.

(11) Margulies, E. A.; Logsdon, J. L.; Miller, C. E.; Ma, L.; Simonoff, E.; Young, R. M.; Schatz, G. C.; Wasielewski, M. R. Direct Observation of a Charge-Transfer State Preceding High-Yield Singlet Fission in Terrylenediimide Thin Films. *J. Am. Chem. Soc.* **2017**, *139* (2), 663–671.

(12) Pensack, R. D.; Tilley, A. J.; Grieco, C.; Purdum, G. E.; Ostroumov, E. E.; Granger, D. B.; Oblinsky, D. G.; Dean, J. C.; Doucette, G. S.; Asbury, J. B.; Loo, Y.-L.; Seferos, D. S.; Anthony, J. E.; Scholes, G. D. Striking the Right Balance of Intermolecular Coupling for High-Efficiency Singlet Fission. *Chem. Sci.* **2018**, *9* (29), 6240–6259.

(13) Ma, L.; Zhang, K.; Kloc, C.; Sun, H.; Michel-Beyerle, M. E.; Gurzadyan, G. G. Singlet Fission in Rubrene Single Crystal: Direct Observation by Femtosecond Pump–Probe Spectroscopy. *Phys. Chem. Chem. Phys.* **2012**, *14* (23), 8307.

(14) Rao, A.; Friend, R. H. Harnessing Singlet Exciton Fission to Break the Shockley–Queisser Limit. *Nat. Rev. Mater.* **2017**, *2* (11), 17063.

(15) Tayebjee, M. J. Y.; Gray-Weale, A. A.; Schmidt, T. W. Thermodynamic Limit of Exciton Fission Solar Cell Efficiency. *J. Phys. Chem. Lett.* **2012**, *3* (19), 2749–2754.

(16) Dexter, D. L. Two Ideas on Energy Transfer Phenomena: Ion-Pair Effects Involving the OH Stretching Mode, and Sensitization of Photovoltaic Cells. *J. Lumin.* **1979**, *18*, 779–784.

(17) Hanna, M. C.; Nozik, A. J. Solar Conversion Efficiency of Photovoltaic and Photoelectrolysis Cells with Carrier Multiplication Absorbers. *J Appl Phys* **2006**, *100* (7), 074510.

(18) Hirst, L. C.; Ekins-Daukes, N. J. Fundamental Losses in Solar Cells. *Prog. Photovolt. Res. Appl.* **2011**, *19* (3), 286–293.

(19) Daiber, B.; van den Hoven, K.; Futscher, M. H.; Ehrler, B. Realistic Efficiency Limits for Singlet-Fission Silicon Solar Cells. *ACS Energy Lett.* **2021**, *6* (8), 2800–2808.

(20) Peumans, P.; Yakimov, A.; Forrest, S. R. Small Molecular Weight Organic Thin-Film Photodetectors and Solar Cells. *J. Appl. Phys.* **2003**, *93* (7), 3693–3723.

(21) Zhang, Y.-H. P. A Sweet Out-of-the-Box Solution to the Hydrogen Economy: Is the Sugar-Powered Car Science Fiction? *Energy Environ. Sci.* **2009**, *2* (3), 272–282

(22) Mohan, M.; Nandal, V.; Paramadam, S.; Reddy, K. P.; Ramkumar, S.; Agarwal, S.; Gopinath, C. S.; Nair, P. R.; Namboothiry, M. A. G. Efficient Organic Photovoltaics with Improved Charge Extraction and High Short-Circuit Current. *J. Phys. Chem. C* **2017**, *121* (10), 5523–5530.

(23) Ye, L.; Zhao, Y.; Xu, R.; Li, S.; Zhang, C.; Li, H.; Zhu, H. Above 100% Efficiency Photocharge Generation in Monolayer Semiconductors by Singlet Fission Sensitization. *J. Am. Chem. Soc.* **2023**, *145* (48), 26257–26265.

(24) Congreve, D. N.; Lee, J.; Thompson, N. J.; Hontz, E.; Yost, S. R.; Reusswig, P. D.; Bahlke, M. E.; Reineke, S.; Van Voorhis, T.; Baldo, M. A. External Quantum Efficiency Above 100% in a Singlet-Exciton-Fission–Based Organic Photovoltaic Cell. *Science* **2013**, *340* (6130), 334–337.

(25) Yang, L.; Tabachnyk, M.; Bayliss, S. L.; Böhm, M. L.; Broch, K.; Greenham, N. C.; Friend, R. H.; Ehrler, B. Solution-Processable Singlet Fission Photovoltaic Devices. *Nano Lett.* **2015**, *15* (1), 354–358.

(26) Tabachnyk, M.; Ehrler, B.; Bayliss, S.; Friend, R. H.; Greenham, N. C. Triplet Diffusion in Singlet Exciton Fission Sensitized Pentacene Solar Cells. *Appl. Phys. Lett.* **2013**, *103*, 153302.

(27) Poletayev, A. D.; Clark, J.; Wilson, M. W. B.; Rao, A.; Makino, Y.; Hotta, S.; Friend, R. H. Triplet Dynamics in Pentacene Crystals: Applications to Fission-Sensitized Photovoltaics. *Adv. Mater.* **2014**, *26* (6), 919–924.

(28) Mikhnenko, O. V.; Ruiter, R.; Blom, P. W. M.; Loi, M. A. Direct Measurement of the Triplet Exciton Diffusion Length in Organic Semiconductors. *Phys. Rev. Lett.* **2012**, *108* (13), 137401.

(29) Kalinowski, J., Godlewski, J., Stizza, S., Davoli, I., & Manchini, G. Optical Constants of Tetracene Single Crystal within the First Absorption Band. *Molecular Crystals and Liquid Crystals Incorporating Nonlinear Optics* **1989***, 166* (1), 233–244.

(30) Irkhin, P.; Ryasnyanskiy, A.; Koehler, M.; Biaggio, I. Absorption and Photoluminescence Spectroscopy of Rubrene Single Crystals. *Phys. Rev. B* **2012**, *86* (8), 085143.

(31) Birech, Z.; Schwoerer, M.; Schmeiler, T.; Pflaum, J.; Schwoerer, H. Ultrafast Dynamics of Excitons in Tetracene Single Crystals. *J. Chem. Phys.* **2014**, *140* (11), 114501.

(32) Schlenker, C. W.; Thompson, M. E. The Molecular Nature of Photovoltage Losses in Organic Solar Cells. *Chem. Commun.* **2011**, *47* (13), 3702–3716.

(33) Thompson, N. J.; Congreve, D. N.; Goldberg, D.; Menon, V. M.; Baldo, M. A. Slow Light Enhanced Singlet Exciton Fission Solar Cells with a 126% Yield of Electrons per Photon. *Appl. Phys. Lett.* **2013**, *103* (26), 263302.

(34) Pace, N. A.; Arias, D. H.; Granger, D. B.; Christensen, S.; Anthony, J. E.; Johnson, J. C. Dynamics of Singlet Fission and Electron Injection in Self-Assembled Acene Monolayers on Titanium Dioxide. *Chem. Sci.* **2018**, *9* (11), 3004–3013.

(35) Schrauben, J. N.; Zhao, Y.; Mercado, C.; Dron, P. I.; Ryerson, J. L.; Michl, J.; Zhu, K.; Johnson, J. C. Photocurrent Enhanced by Singlet Fission in a Dye-Sensitized Solar Cell. *ACS Appl. Mater. Interfaces* **2015**, *7* (4), 2286–2293.

(36) Smith, M. B.; Michl, J. Recent Advances in Singlet Fission. *Annu. Rev. Phys. Chem.* **2013**, *64* (1), 361–386.

(37) Miyata, K.; Conrad-Burton, F. S.; Geyer, F. L.; Zhu, X.-Y. Triplet Pair States in Singlet Fission. *Chem. Rev.* **2019**, *119* (6), 4261–4292.

(38) Bayliss, S. L.; Chepelianskii, A. D.; Sepe, A.; Walker, B. J.; Ehrler, B.; Bruzek, M. J.; Anthony, J. E.; Greenham, N. C. Geminate and Nongeminate Recombination of Triplet Excitons Formed by Singlet Fission. *Phys. Rev. Lett.* **2014**, *112* (23), 238701.

(39) Dexter, D. L. A Theory of Sensitized Luminescence in Solids. *J. Chem. Phys.* **1953**, *21* (5), 836–850.

(40) Li, H.; Li, C.; Duan, L.; Qiu, Y. Charge Transport in Amorphous Organic Semiconductors: Effects of Disorder, Carrier Density, Traps, and Scatters. *Isr. J. Chem.* **2014**, *54* (7), 918–926.

(41) Wong, C. Y.; Cotts, B. L.; Wu, H.; Ginsberg, N. S. Exciton Dynamics Reveal Aggregates with Intermolecular Order at Hidden Interfaces in Solution-Cast Organic Semiconducting Films. *Nat. Commun.* **2015**, *6* (1), 5946.

(42) Shi, K.; Healy, A. T.; Curtin, I. J.; Zhang, T.; Blank, D. A.; Holmes, R. J. Impact of Grain Boundaries on Triplet Exciton Diffusion in Organic Singlet-Fission Materials. *J. Phys. Chem. C* **2022**, *126* (10), 4792–4798.

(43) Lunt, R. R.; Benziger, J. B.; Forrest, S. R. Relationship between Crystalline Order and Exciton Diffusion Length in Molecular Organic Semiconductors. *Adv. Mater.* **2010**, *22* (11), 1233–1236.

(44) Hestand, N. J.; Tempelaar, R.; Knoester, J.; Jansen, T. L. C.; Spano, F. C. Exciton Mobility Control through Sub − Å Packing Modifications in Molecular Crystals. *Phys. Rev. B* **2015**, *91* (19), 195315.

(45) Volek, T. S.; Armstrong, Z. T.; Sowa, J. K.; Wilson, K. S.; Bohlmann Kunz, M.; Bera, K.; Koble, M.; Frontiera, R. R.; Rossky, P. J.; Zanni, M. T.; Roberts, S. T. Structural Disorder

at the Edges of Rubrene Crystals Enhances Singlet Fission. *J. Phys. Chem. Lett.* **2023**, *14* (50), 11497–11505.

(46) Jones, A. C.; Kearns, N. M.; Ho, J.-J.; Flach, J. T.; Zanni, M. T. Impact of Non-Equilibrium Molecular Packings on Singlet Fission in Microcrystals Observed Using 2D White-Light Microscopy. *Nat. Chem.* **2020**, *12* (1), 40–47.

(47) Irkhin, P.; Biaggio, I. Direct Imaging of Anisotropic Exciton Diffusion and Triplet Diffusion Length in Rubrene Single Crystals. *Phys. Rev. Lett.* **2011**, *107* (1), 017402.

(48) Najafov, H.; Lee, B.; Zhou, Q.; Feldman, L. C.; Podzorov, V. Observation of Long-Range Exciton Diffusion in Highly Ordered Organic Semiconductors. *Nat. Mater.* **2010**, *9* (11), 938–943.

(49) Radiunas, E.; Dapkevičius, M.; Raišys, S.; Kazlauskas, K. Triplet and Singlet Exciton Diffusion in Disordered Rubrene Films: Implications for Photon Upconversion. *Phys. Chem. Chem. Phys.* **2022**, *24* (39), 24345–24352.

(50) Lloyd, S.; Mohseni, M. Symmetry-Enhanced Supertransfer of Delocalized Quantum States. *New J. Phys.* **2010**, *12* (7), 075020.

(51) Palacios, M. A.; De Weerd, F. L.; Ihalainen, J. A.; Van Grondelle, R.; Van Amerongen, H. Superradiance and Exciton (De)Localization in Light-Harvesting Complex II from Green Plants? *J. Phys. Chem. B* **2002**, *106* (22), 5782–5787.

(52) Fidder, H.; Knoester, J.; Wiersma, D. A. Optical Properties of Disordered Molecular Aggregates: A Numerical Study. *J. Chem. Phys.* **1991**, *95* (11), 7880–7890.

(53) Mikhnenko, O. V.; Blom, P. W. M.; Nguyen, T.-Q. Exciton Diffusion in Organic Semiconductors. *Energy Environ. Sci.* **2015**, *8* (7), 1867–1888.

(54) Zhu, T.; Wan, Y.; Guo, Z.; Johnson, J.; Huang, L. Two Birds with One Stone: Tailoring Singlet Fission for Both Triplet Yield and Exciton Diffusion Length. *Adv. Mater.* **2016**, *28* (34), 7539–7547.

(55) Wan, Y.; Guo, Z.; Zhu, T.; Yan, S.; Johnson, J.; Huang, L. Cooperative Singlet and Triplet Exciton Transport in Tetracene Crystals Visualized by Ultrafast Microscopy. *Nat. Chem.* **2015**, *7* (10), 785–792.

(56) Tamura, H.; Azumaya, K.; Ishikita, H. Long-Range Exciton Diffusion via Singlet Revival Mechanism. *J. Phys. Chem. Lett.* **2019**, *10* (24), 7623–7628.

(57) Akselrod, G. M.; Deotare, P. B.; Thompson, N. J.; Lee, J.; Tisdale, W. A.; Baldo, M. A.; Menon, V. M.; Bulović, V. Visualization of Exciton Transport in Ordered and Disordered Molecular Solids. *Nat. Commun.* **2014**, *5* (1), 3646.

(58) Berghuis, A. M.; Raziman, T. V.; Halpin, A.; Wang, S.; Curto, A. G.; Rivas, J. G. Effective Negative Diffusion of Singlet Excitons in Organic Semiconductors. *J. Phys. Chem. Lett.* **2021**, *12* (4), 1360–1366.

(59) Cvrčková, O.; Ciganek, M. Photostability of Polycyclic Aromatic Hydrocarbons (PAHs) and Nitrated Polycyclic Aromatic Hydrocarbons (NPAHs) in Dichloromethane and Isooctane Solutions *Polycycl. Aromat. Compd.* **2005**, *25* (2), 141–156.

(60) Kaur, I.; Jia, W.; Kopreski, R. P.; Selvarasah, S.; Dokmeci, M. R.; Pramanik, C.; McGruer, N. E.; Miller, G. P. Substituent Effects in Pentacenes: Gaining Control over HOMO−LUMO Gaps and Photooxidative Resistances. *J. Am. Chem. Soc.* **2008**, *130* (48), 16274–16286.

(61) Bruzek, M. J.; Anthony, J. E. Synthesis and Optical Properties of Dioxolane-Functionalized Hexacenes and Heptacenes. *Org. Lett.* **2014**, *16* (13), 3608–3610.

(62) Burgdorff, C.; Ehrhardt, S.; Löehmannsröeben, H. G. Photophysical Properties of Tetracene Derivatives in Solution. 2. Halogenated Tetracene Derivatives. *J. Phys. Chem.* **1991**, *95* (11), 4246–4249.

(63) Würthner, F. Perylene Bisimide Dyes as Versatile Building Blocks for Functional Supramolecular Architectures. *Chem Commun* **2004**, *14*, 1564–1579.

(64) Dubey, R. K.; Würthner, F. Playing Lego with Perylene Dyes. *Nat. Chem.* **2023**, *15* (6), 884–884.

(65) Löhmannsröben, H. G.; Langhals, H. Laser Performance of Perylenebis (Dicarboximide) Dyes with Long Secondary Alkyl Chains. *Appl. Phys. B Photophysics Laser Chem.* **1989**, *48* (6), 449–452.

(66) Huang, C.; Barlow, S.; Marder, S. R. Perylene-3,4,9,10-Tetracarboxylic Acid Diimides: Synthesis, Physical Properties, and Use in Organic Electronics. *J. Org. Chem.* **2011**, *76* (8), 2386–2407.

(67) Ford, W. E.; Kamat, P. V. Photochemistry of 3,4,9,10-Perylenetetracarboxylic Dianhydride Dyes. 3. Singlet and Triplet Excited-State Properties of the Bis(2,5-Di-Tert-Butylphenyl)Imide Derivative. *J. Phys. Chem.* **1987**, *91* (25), 6373–6380.

(68) Langhals, H. Spectroscopic Properties of New and Convenient Standards for Measuring Ñuorescence Quantum Yields. *J. Chem. Soc.*, **1998**, *94* (19), 2919–2922.

(69) Nakazono, S.; Easwaramoorthi, S.; Kim, D.; Shinokubo, H.; Osuka, A. Synthesis of Arylated Perylene Bisimides through C−H Bond Cleavage under Ruthenium Catalysis. *Org. Lett.* **2009**, *11* (23), 5426–5429.

(70) Fukuzumi, S.; Ohkubo, K.; Ortiz, J.; Gutiérrez, A. M.; Fernández-Lázaro, F.; Sastre-Santos, A. Control of Photoinduced Electron Transfer in Zinc Phthalocyanine-Perylenediimide Dyad and Triad by the Magnesium Ion. *J. Phys. Chem. A* **2008**, *112* (43), 10744–10752.

(71) Le, A. K.; Bender, J. A.; Arias, D. H.; Cotton, D. E.; Johnson, J. C.; Roberts, S. T. Singlet Fission Involves an Interplay between Energetic Driving Force and Electronic Coupling in Perylenediimide Films. *J. Am. Chem. Soc.* **2018**, *140* (2), 814–826.

(72) Hong, Y.; Kim, J.; Kim, W.; Kaufmann, C.; Kim, H.; Würthner, F.; Kim, D. Efficient Multiexciton State Generation in Charge-Transfer-Coupled Perylene Bisimide Dimers via Structural Control. *J. Am. Chem. Soc.* **2020**, *142* (17), 7845–7857.

(73) Aulin, Y. V.; Felter, K. M.; Günbas, D. D.; Dubey, R. K.; Jager, W. F.; Grozema, F. C. Morphology-Independent Efficient Singlet Exciton Fission in Perylene Diimide Thin Films. *ChemPlusChem* **2018**, *83* (4), 230–238.

(74) Mizuguchi, J.; Tojo, K. Electronic Structure of Perylene Pigments as Viewed from the Crystal Structure and Excitonic Interactions. *J. Phys. Chem. B* **2002**, *106* (4), 767–772.

(75) Mizuguchi, J. *N*,*N*'-Bis(2-Phenethyl)Perylene-3,4:9,10-Bis(Dicarboximide). *Acta Crystallogr. C* **1998**, *54* (10), 1479–1481.

(76) Hadicke, E.; Graser, F. Structures of Eleven Perylene-3,4:9,10-Bis(Dicarboximide) Pigments. *Acta Crystallogr.* **1986**, *C42*, 189–195.

(77) Hadicke, E.; Graser, F. Structures of Three Perylene-3,4:9,10-Bis(Dicarboximide) Pigments. *Acta Crystallogr.* **1986**, *C42*, 195–198.

(78) Klebe, G.; Graser, F.; Hädicke, E.; Berndt, J. Crystallochromy as a Solid-State Effect: Correlation of Molecular Conformation, Crystal Packing and Colour in Perylene-3,4:9,10-Bis(Dicarboximide) Pigments. *Acta Crystallogr. B* **1989**, *45* (1), 69–77.

(79) Renaud, N.; Grozema, F. C. Intermolecular Vibrational Modes Speed Up Singlet Fission in Perylenediimide Crystals. *J. Phys. Chem. Lett.* **2015**, *6* (3), 360–365.

(80) Mirjani, F.; Renaud, N.; Gorczak, N.; Grozema, F. C. Theoretical Investigation of Singlet Fission in Molecular Dimers: The Role of Charge Transfer States and Quantum Interference. *J. Phys. Chem. C* **2014**, *118* (26), 14192–14199.

(81) Kim, Y.-J.; Lee, Y.; Park, K.; Ahn, C. W.; Jung, H.-T.; Jeon, H.-J. Hierarchical Self-Assembly of Perylene Diimide (PDI) Crystals. *J. Phys. Chem. Lett.* **2020**, *11* (10), 3934–3940.

(82) Mizuguchi, J. Electronic Characterization of N,N′-Bis(2-Phenylethyl)Perylene-3,4:9, 10-Bis(Dicarboximide) and Its Application to Optical Disks. *J. Appl. Phys.* **1998**, *84* (8), 4479–4486.

(83) Jones, C. G.; Martynowycz, M. W.; Hattne, J.; Fulton, T. J.; Stoltz, B. M.; Rodriguez, J. A.; Nelson, H. M.; Gonen, T. The CryoEM Method MicroED as a Powerful Tool for Small Molecule Structure Determination. *ACS Cent. Sci.* **2018**, *4* (11), 1587–1592.

(84) Levine, A. M.; He, G.; Bu, G.; Ramos, P.; Wu, F.; Soliman, A.; Serrano, J.; Pietraru, D.; Chan, C.; Batteas, J. D.; Kowalczyk, M.; Jang, S. J.; Nannenga, B. L.; Sfeir, M. Y.; R. Tsai, E. H.; Braunschweig, A. B. Efficient Free Triplet Generation Follows Singlet Fission in Diketopyrrolopyrrole Polymorphs with Goldilocks Coupling. *J. Phys. Chem. C* **2021**, *125* (22), 12207–12213.

(85) Levine, A. M.; Bu, G.; Biswas, S.; Tsai, E. H. R.; Braunschweig, A. B.; Nannenga, B. L. Crystal Structure and Orientation of Organic Semiconductor Thin Films by Microcrystal Electron Diffraction and Grazing-Incidence Wide-Angle X-Ray Scattering. *Chem. Commun.* **2020**, *56* (30), 4204–4207.

(86) Felter, K. M.; Grozema, F. C. Singlet Fission in Crystalline Organic Materials: Recent Insights and Future Directions. *J. Phys. Chem. Lett.* **2019**, *10* (22), 7208–7214.

(87) Berkelbach, T. C.; Hybertsen, M. S.; Reichman, D. R. Microscopic Theory of Singlet Exciton Fission. II. Application to Pentacene Dimers and the Role of Superexchange. *J. Chem. Phys.* **2013**, *138* (11), 114103.

(88) Farag, M. H.; Krylov, A. I. Singlet Fission in Perylenediimide Dimers. *J. Phys. Chem. C* **2018**, *122* (45), 25753–25763.

(89) Ryerson, J. L.; Schrauben, J. N.; Ferguson, A. J.; Sahoo, S. C.; Naumov, P.; Havlas, Z.; Michl, J.; Nozik, A. J.; Johnson, J. C. Two Thin Film Polymorphs of the Singlet Fission Compound 1,3-Diphenylisobenzofuran. *J. Phys. Chem. C* **2014**, *118* (23), 12121–12132.

(90) Buchanan, E. A.; Johnson, J. C.; Tan, M.; Kaleta, J.; Shtukenberg, A. G.; Bateman, G.; Benedict, J. B.; Kobayashi, S.; Wen, J.; Kahr, B.; Císařová, I.; Michl, J. Competing Singlet Fission and Excimer Formation in Solid Fluorinated 1,3-Diphenylisobenzofurans. *J. Phys. Chem. C* **2021**, *125* (49), 27058–27071.

(91) Kazmaier, P. M.; Hoffmann, R. A Theoretical Study of Crystallochromy. Quantum Interference Effects in the Spectra of Perylene Pigments. *J. Am. Chem. Soc.* **1994**, *116* (21), 9684–9691.

(92) Austin, A.; Hestand, N. J.; McKendry, I. G.; Zhong, C.; Zhu, X.; Zdilla, M. J.; Spano, F. C.; Szarko, J. M. Enhanced Davydov Splitting in Crystals of a Perylene Diimide Derivative. *J. Phys. Chem. Lett.* **2017**, *8* (6), 1118–1123.

(93) Hestand, N. J.; Spano, F. C. Molecular Aggregate Photophysics beyond the Kasha Model: Novel Design Principles for Organic Materials. *Acc. Chem. Res.* **2017**, *50* (2), 341–350.

(94) Yamagata, H.; Maxwell, D. S.; Fan, J.; Kittilstved, K. R.; Briseno, A. L.; Barnes, M. D.; Spano, F. C. HJ-Aggregate Behavior of Crystalline 7,8,15,16-Tetraazaterrylene: Introducing a New Design Paradigm for Organic Materials. *J. Phys. Chem. C* **2014**, *118* (49), 28842–28854.

(95) Spano, F. C. Absorption and Emission in Oligo-Phenylene Vinylene Nanoaggregates: The Role of Disorder and Structural Defects. *J. Chem. Phys.* **2002**, *116* (13), 5877–5891.

(96) Motamen, S.; Raithel, D.; Hildner, R.; Rahimi, K.; Jarrosson, T.; Serein-Spirau, F.; Simon, L.; Reiter, G. Revealing Order and Disorder in Films and Single Crystals of a Thiophene-Based Oligomer by Optical Spectroscopy. *ACS Photonics* **2016**, *3* (12), 2315–2323.

(97) Voigt, M.; Langner, A.; Schouwink, P.; Lupton, J. M.; Mahrt, R. F.; Sokolowski, M. Picosecond Time Resolved Photoluminescence Spectroscopy of a Tetracene Film on Highly Oriented Pyrolytic Graphite: Dynamical Relaxation, Trap Emission, and Superradiance. *J. Chem. Phys.* **2007**, *127* (11), 114705.

(98) Gross, N.; Kuhs, C. T.; Ostovar, B.; Chiang, W.-Y.; Wilson, K. S.; Volek, T. S.; Faitz, Z. M.; Carlin, C. C.; Dionne, J. A.; Zanni, M. T.; Gruebele, M.; Roberts, S. T.; Link, S.; Landes, C. F. Progress and Prospects in Optical Ultrafast Microscopy in the Visible Spectral Region: Transient Absorption and Two-Dimensional Microscopy. *J. Phys. Chem. C* **2023**, *127* (30), 14557–14586.

(99) Qian, H.; Sheetz, M. P.; Elson, E. L. Single Particle Tracking. Analysis of Diffusion and Flow in Two-Dimensional Systems. *Biophys. J.* **1991**, *60* (4), 910–921.

(100) Michalet, X. Mean Square Displacement Analysis of Single-Particle Trajectories with Localization Error: Brownian Motion in an Isotropic Medium. *Phys. Rev. E* **2010**, *82* (4), 041914.

(101) Crank, J.; Nicolson, P. A Practical Method for Numerical Evaluation of Solutions of Partial Differential Equations of the Heat-Conduction Type. *Math. Proc. Camb. Philos. Soc.* **1947**, *43* (1), 50–67.

(102) Williams, M. L.; Schlesinger, I.; Ramirez, C. E.; Jacobberger, R. M.; Brown, P. J.; Young, R. M.; Wasielewski, M. R. Effect of Crystallinity on Endoergic Singlet Fission in Perylenediimide Single Crystals and Polycrystalline Films. *J. Phys. Chem. C* **2022**, *126* (25), 10287–10297.

(103) Gregg, B. A.; Sprague, J.; Peterson, M. W. Long-Range Singlet Energy Transfer in Perylene Bis(Phenethylimide) Films. *J. Phys. Chem. B* **1997**, *101* (27), 5362–5369.

(104) Adams, D. M.; Kerimo, J.; O'Connor, D. B.; Barbara, P. F. Spatial Imaging of Singlet Energy Migration in Perylene Bis(Phenethylimide) Thin Films. *J. Phys. Chem. A* **1999**, *103* (49), 10138–10143.

(105) Förster, T. Zwischenmolekulare Energiewanderung Und Fluoreszenz. *Naturwissenschaften* **19346**, *27* (0), 7–17.

(106) Förster, T. 10th Spiers Memorial Lecture. Transfer Mechanisms of Electronic Excitation. *Discuss Faraday Soc* **1959**, *27* (0), 7–17.

(107) Suna, A. Kinematics of Exciton-Exciton Annihilation in Molecular Crystals. *Phys. Rev. B* **1970**, *1* (4), 1716–1739.